



The role of defects and critical pore size analysis in the fatigue response of additively manufactured IN718 via crystal plasticity

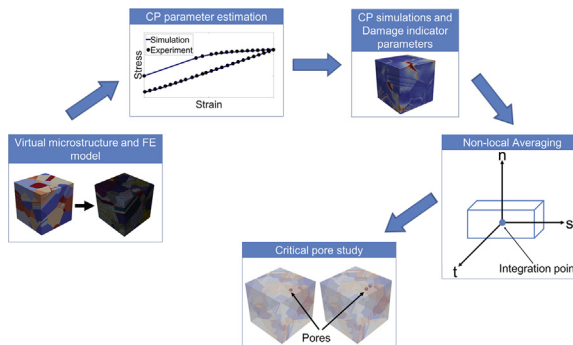
Veerappan Prithivirajan, Michael D. Sangid *

School of Aeronautics and Astronautics, Purdue University, 701 W. Stadium Ave., West Lafayette, IN 47907, USA

HIGHLIGHTS

- Critical porosity is estimated in additively manufactured IN718 via crystal plasticity.
- Porosity is characterized using high resolution tomography.
- Non-local damage indicator parameters identify the location of fatigue crack initiation.
- The critical pore size is 20 μm in IN718 with average grain size of 48 μm .
- From the tomography characterization, 1% of the pores may result in failure.

GRAPHICAL ABSTRACT



ARTICLE INFO

Article history:

Received 24 February 2018
Received in revised form 30 March 2018
Accepted 9 April 2018
Available online 14 April 2018

Keywords:

Selective laser melting
IN718
Critical pore size
Crystal plasticity
Fatigue

ABSTRACT

The inherent defects associated with materials produced by selective laser melting (SLM) limits their usage in safety-critical applications. In our work, a crystal plasticity (CP) based framework is developed to identify the critical porosity characteristics, which quantifies the limiting scenarios of fatigue crack initiation at a pore rather than the crystallographic features. 3D virtual microstructures are developed based on the characterization of SLM IN718 for use in the CP simulations. Damage indicator parameters, such as the plastic strain accumulation, elastic stress anisotropy, resolved shear stress and triaxiality, obtained from the CP simulations are used to identify the most probable locations of crack initiation. Pores are explicitly added to the microstructure instantiations in a systematic manner by varying the size, location, and proximity between pores. The critical pore size is defined as the size beyond which the location of crack nucleation transitions from crystallographic features to the pore vicinity, which is determined to be 20 μm in the material of interest with an average grain size of 48 μm . This work is beneficial in qualifying SLM materials given the natural porosity inherent to the manufacturing process, by reducing the number of fatigue experiments.

© 2018 Elsevier Ltd. All rights reserved.

1. Introduction

Defects play a crucial role in governing the mechanical response and the failure mechanisms of structural materials. Selective laser melting

(SLM) [1,2], an additive manufacturing (AM) technique, produces various defects [3–10], which restrict the adoption of these materials in safety-critical applications. Hence, it is essential to understand the role of defects on the mechanical behavior to inform process parameter optimization, experimental characterization, and qualification. The focus of this paper is on the influence of porosity on fatigue crack initiation of a Ni-base superalloy, Inconel 718 (IN 718), manufactured by SLM.

* Corresponding author.

E-mail address: msangid@purdue.edu (M.D. Sangid).



Porosity is a potential source of fatigue crack initiation in both AM [6,11–13] and in conventionally manufactured materials [14–19]. Experimental observations based on fractography analysis have shown that the characteristics of a crack-initiating pore in fatigue are related to the pore size and the proximity to the surface or an adjacent pore. Couper et al. have shown that the pore size is more critical than pore volume fraction in connection with the fatigue behavior of a cast aluminum alloy [14]. Wang et al. have experimentally estimated a critical pore size by comparing the fatigue lives of fully dense and porous microstructures of a cast aluminum alloy [15]. Additionally, researchers have shown that fatigue cracks initiate from near-surface and surface pores [12,18,20]. Furthermore, Danner et al. [16] and Pang et al. [18] have shown that a pore cluster is a prominent location of crack initiation due to interaction effects. As of now, a robust understanding of the limiting cases of porosity in terms of pore size and clustering of pores for SLM materials is still elusive.

Computed tomography (CT) is a non-destructive method used in the detection and characterization of micro-pores in a material, and in the analysis of fatigue crack initiation. 3D reconstruction of the pores in the material microstructure using CT is shown in [6,10,21–25]. The detection of a pore is dependent on the resolution of the tomography set-up which varies from sub-micron to sub-millimeter. In this paper, two different resolutions per voxel are used, namely, 0.65 μm and 30 μm (Section 2). However, to make an informed optimal choice of a tomography set-up, prior knowledge of the minimum pore size that affects the fatigue properties is essential.

Extensive specimen testing under fatigue loading combined with fractography analysis or CT is one of the ways to identify limiting porosity. However, due to the time and cost involved, a more feasible alternative is to make use of numerical modeling and simulation. There has also been a growing need for predictive models in rapid qualification and certification of SLM materials [26], which is the focus of the present work.

Some of the early work on the role of porosity towards the mechanical behavior involved the development of analytical models to understand ductile failure using continuum plasticity theory [27–32]. These pioneering works have played a significant role in understanding the deformation behavior of materials with pores. Recent studies explicitly account for pores within a finite element (FE) model as it allows for more complex geometry and material description. Gall et al. [33] and Fan et al. [34] studied the plastic strain localization around a pore using a continuum plasticity framework in an idealized 2D-FE analysis. Gall et al. found that pore size and loading ratios have a significant influence on the strain localization [33]. In addition, Fan et al. [34] and Xu et al. [35] obtained the trends on strain localization by varying the distance of the pore from the surface and spacing of the pore cluster. Gall et al. [33] and Baicchi et al. [36] showed that the pore shape has minimal effect on the plastic strain. All of the above studies model the deformation by placing the pore in a homogenized matrix [33–36] and thereby ignoring the effects of spatial inhomogeneity of a polycrystalline microstructure having various grain morphologies and orientations, which can significantly impact the results.

A few studies have been conducted by placing a pore within a heterogeneous matrix explicitly accounting for microstructural attributes. Gao et al. have studied the variation in plastic strain localization around a pore in a bi-crystal by varying the crystallographic orientation of the grains [37]. Carroll et al. have modeled the pore in a polycrystalline microstructure with a large number of grains having random orientations using 2D CP-FE simulations. They conducted the study using different pore sizes and concluded that the local microstructure profoundly influences the strain localization only when the pore has a size comparable to or less than the average grain size, and it has nearly no influence if the pore is significantly larger than the average grain size [38]. Battaile et al. extended the previous study [38] by performing a variability study on the peak plastic strain for different pore sizes using multiple instantiations. Within each microstructure instantiation, the crystallographic

orientation of the grains is varied and grain morphology is held constant. Additionally, they showed that a sub-grain pore in a polycrystalline matrix localizes more plastic strain than when placed in an isotropic matrix [39]. The aforementioned studies [37–39] deal with monotonic (tensile) loading and hence do not provide adequate insights on the deformation behavior of pores subjected to cyclic loading. The cyclic deformation captures the effect of reverse plasticity, and stress redistribution that is of prime importance to the study of fatigue crack nucleation.

In this work, the authors propose a CP-FE based modeling framework to predict the limiting cases of porosity (pore size and proximity within a pore cluster) affecting the fatigue crack initiation of SLM IN718, which also addresses an existing gap in the current literature. Cyclic simulations are performed for multiple instantiations of the 3D microstructure containing pores of varying pore sizes, locations relative to the surrounding microstructure, and proximity between adjacent pores. Multiple instantiations in this study allow variation in both crystallographic orientation and grain morphology to understand the resulting sensitivity with different microstructures. Within this paper, Section 2 describes the characterization of the material and porosity, Section 3 details about the modeling framework including the description of CP-FE simulations, Section 4 presents the problem formulation with the results, and Sections 5 and 6 provide the discussions and conclusions of this work, respectively.

2. Material and characterization of microstructure and defects

The material of interest in this study is IN718, produced by SLM. The material was produced at Penn State University's Center for Innovative Materials Processing through Direct Digital Deposition (CIMP-3D) via an EOSINT M280 system [40]. Samples were produced in bulk blocks (from which coupons would be extracted) and net-shape dogbone specimens, both of which were built in the vertical orientation. The samples underwent a stress relief heat treatment prior to being removed from the build plate (1065 °C for 1.5 h followed by a two-bar argon cooling). Afterwards, the parts underwent vacuum homogenization (1177 °C for 1 h followed by two bar argon cooling at 38 °C/h to below 538 °C), vacuum solution heat treatment (982 °C for 1 h followed by gas fan cooling with argon to below 149 °C), and a two-part vacuum aging process (718 °C for 8 h, furnace cooled to 621 °C and held for 18 h, and then gas fan cooled with argon to below 149 °C). It should be noted that the samples did not undergo hot isostatic pressing. The heat treatment was adequate to form γ' and γ'' precipitates, as the major strengthening mechanism in this alloy, as well as a large fraction of annealing twins. The reader is referred to [41] for a detailed electron microscopy analysis of this material. To identify grain attributes, several coupons of the material were characterized via electron backscatter diffraction (EBSD) analysis using a Phillips XL-40 SEM with an EDAX EBSD camera and associated TSL data collection and analysis software. More details on the scan parameters and EBSD analysis are available in [42]. The pertinent microstructural attributes used in this study are a grain size of 52.7 μm with a standard deviation of 52.2 μm , random texture, and twin area fraction of 0.52.

To characterize the defects inherent in the material as a result of the SLM processing, detailed tomography evaluation and analysis were conducted at two different length-scales in terms of scanned volume and resolution of the tomograms. First, a lower resolution CT characterization was conducted on a GE Phoenix V Tome X M 300 CT System at CIMP-3D. Two types of samples were scanned and reconstructed, including bulk blocks from the build process (50.8 mm by 21.59 mm by 19.05 mm, as shown in Fig. 1a) and net-shape dog-bone specimens (3 mm thick and 50.8 mm in overall length by 8.9 mm in width, while the gauge section is 17.5 mm long by 3.5 mm in width, as shown in Fig. 1b). The CT characterization had a resolution of 30 μm per voxel (as 1680 voxels represented the longest dimension of 50.8 mm). Next, a higher resolution synchrotron based X-ray micro-computed tomography

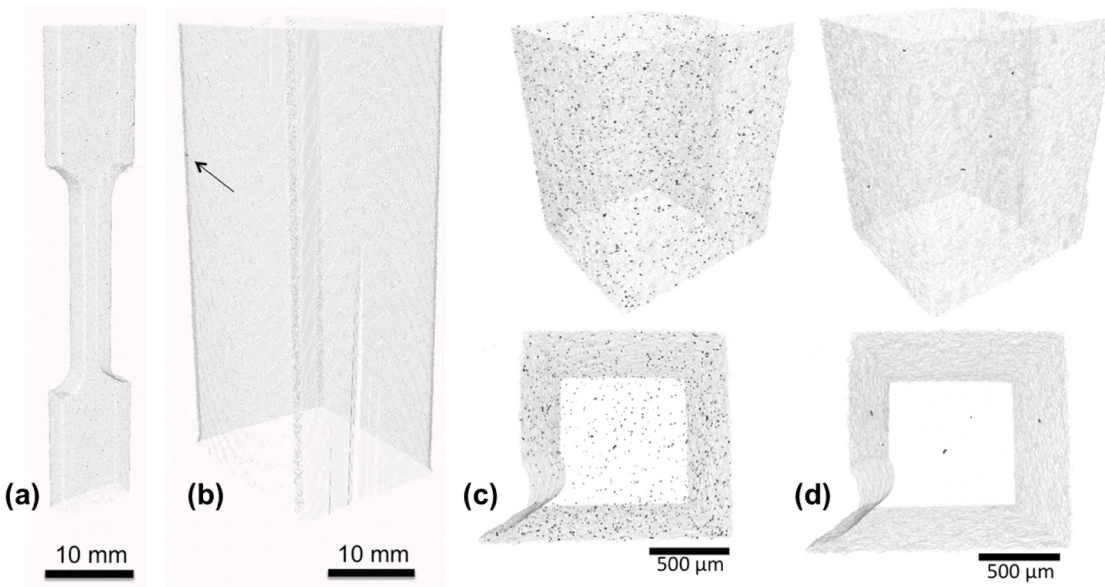


Fig. 1. Tomography reconstruction showing porosity of IN718 for various samples and settings: (a) CT sample of dogbone (b) CT sample of bulk block, (c) μ XSCT sample from bulk – with $5 \times 5 \times 5$ voxel filter, and (d) μ XSCT sample from bulk – with $10 \mu\text{m}$ equivalent diameter filter.

(μ XSCT) was conducted on $10 \text{ mm} \times 1 \text{ mm} \times 1 \text{ mm}$ coupons extracted from the bulk of the blocks at 2-BM of the Advanced Photon Source at Argonne National Laboratory. The μ XSCT characterization consisted of 1500 projections taken over 180° continuously rotated at $1^\circ/\text{s}$ with a 100 ms exposure time in white beam mode. The μ XSCT characterization had a resolution of $0.65 \mu\text{m}$ per voxel (as 1532 voxels represented the longest dimension of 1 mm). Tomographic reconstructions were performed on the acquired radiographs using a gridrec algorithm [43,44] implemented in tomographic data processing software, TomoPy 1.0.0 [45].

Image processing consisted of both thresholding, using the Ostu method [46] and segmentation, which were performed using a combination of ImageJ [47,48] and Avizo 9.2.0 software [49]. The segmented rendered volumes are shown in Fig. 1 to display the porosity. A pore was considered based on the threshold and segmented phase contrast. A reliable volume was determined based on a $2 \times 2 \times 2$ surface connected voxel filter (8 voxel minimum–minimum $1.3 \mu\text{m}$ minimum diameter), whereas a reliable morphology description required a $5 \times 5 \times 5$ surface connected voxel filter (125 voxels minimum–minimum $3.25 \mu\text{m}$ minimum diameter) [22]. Fig. 1c displays the porosity from the μ XSCT characterization with the 125 voxel filter. For visualization, only pores with equivalent diameter of $10 \mu\text{m}$ or larger in the μ XSCT sample are shown in Fig. 1d. As seen in Table 1, the disparity in resolution and scanned volume results in drastically different percentages of porosity. The lower resolution CT scans can capture much larger scanned volumes, but cannot measure small pores that are prevalent in the AM process. Thus, the degree of porosity measured in the μ XSCT characterization is significantly higher than the CT characterization. However, due to the small scanned volume inherent to the μ XSCT technique, it results in low probability of scanning large pores, since an insufficient volume is probed. Moreover, due to the high surface area to

volume ratio of the dogbone specimen, compared to the bulk block, the dogbone specimens contain a significantly larger degree of porosity. The cumulative distribution function (CDF) of the porosity for the different techniques and parts are shown in Fig. 2a, with the 8 voxel filter applied to each dataset. The μ XSCT characterization shows a median pore size of $4 \mu\text{m}$. Moreover, the data was analyzed to determine the minimum distance to an adjacent pore (for each pore analyzed). The minimum pore spacing is shown in Fig. 2b, with the median distance to the closest pore being $\sim 10.5 \mu\text{m}$.

3. Modeling framework

The sequence of steps followed in the critical pore study using CP-FE simulations are represented in Fig. 3. It includes the creation of the 3D virtual microstructures from EBSD characterization data followed by the generation of finite element meshes, CP parameter estimation using a genetic algorithm, cyclic simulations of microstructural models and estimation of damage indicator parameters, application of non-local averaging, and lastly, critical pore analyses to determine limiting cases of porosity. The details of each step are provided in the following sub-sections.

3.1. Virtual microstructures and finite element model

Based on the characterization of the microstructure from EBSD, 3-D virtual microstructures are created as input to the CP-FE simulations. From the EBSD characterization, the information about the microstructural attributes, specifically the grain size, orientation, and grain boundary character distributions (twin area fraction) are obtained. The creation of a virtual microstructure is a multistep iterative process. First, a parent microstructure with grains (slightly bigger than measured) is constructed with the texture representative of the measured value from EBSD, using DREAM.3D [50]. Second, twins (with a width of $\sim 7 \mu\text{m}$ corresponding to EBSD) are segmented along one of the randomly chosen $\langle 111 \rangle$ planes in randomly chosen grains of the parent microstructure using a twin-insertion code [51]. The twins extend throughout the parent grain, and the orientation of the segmented twins is calculated such that the resulting misorientation with the corresponding parent grain is 60° . The process is iterated until an equivalency is achieved between the characterization microstructure attributes and virtual microstructures. The equivalency is attained with

Table 1
Porosity data using μ XSCT and CT.

Sample	Resolution (μm)	Qty	Total Volume (mm^3)	Porosity (%)
μ XSCT	0.65	8	10.4	4.5×10^{-2}
CT-Blocks	30	2	41,878	4.5×10^{-8}
CT-Tensile Specimens	30	3	3960	8.6×10^{-4}

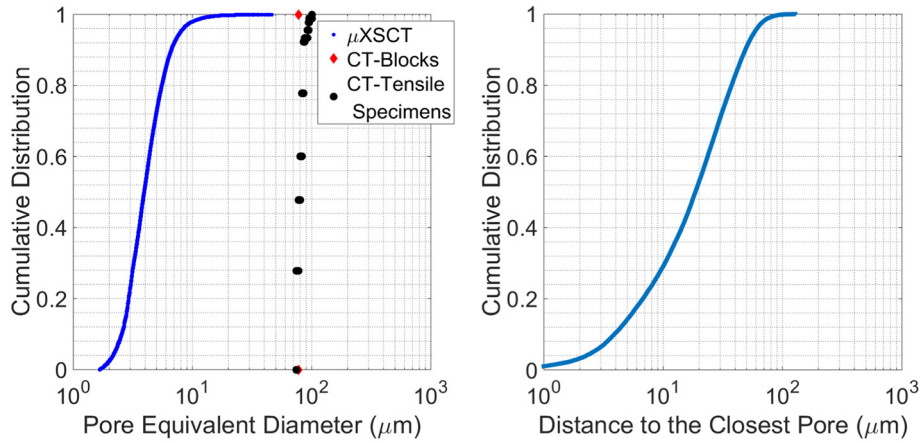


Fig. 2. Porosity data from tomography reconstruction of IN718 (a) Cumulative distribution of pore equivalent diameter and (b) Cumulative distribution of distance to the closest pore.

respect to the mean of the grain size distribution, the twin area fraction and the Taylor factors (a scalar measure of texture). From a sensitivity study, it is found that ~190 grains are needed to have a converged macroscopic stress-strain response. The 3-D virtual microstructures will be referred to as statistical equivalent microstructures (SEMs) hereafter as they represent statistical equivalency in terms of both microstructural attributes and macroscopic stress-strain behavior. A total of 5 SEMs (Fig. 4) are created, and each SEM is a cube of dimension 300 μm . The microstructural statistics of each SEM including the number of grains, twin area fraction and the Taylor factors are given in Table 2.

The surface meshing and grain smoothing of the SEMs are performed using DREAM 3D, and the 3D volume meshing of the SEMs is performed using Gmsh [52]. Linear tetrahedron elements (C3D4) are used. The size of the mesh element, the aspect of volumetric locking, and mesh convergence will be discussed in Section 3.4. As stated, the SEMs have similar macroscopic stress-strain responses (Fig. 5) with the same set of CP parameters. The CP model and parameter estimation are discussed in the next section.

3.2. Crystal plasticity model and parameter estimation

A phenomenological CP model [53–55] is used which considers the 12 FCC slip systems: $\langle 110 \rangle \{111\}$. The model is incorporated in Abaqus using a User-Material subroutine (UMAT). The kinematics of slip is captured using the multiplicative decomposition [56] of the total deformation gradient, F .

$$F = F_e F_p \quad (1)$$

The elastic portion of the deformation gradient, F_e , accounts for the elastic stretch and rotation of the lattice, while the plastic portion of the deformation gradient, F_p , accounts for the crystallographic slip. The plastic velocity gradient, L_p , is related to the shearing rates, $\dot{\gamma}$, on specific slip systems:

$$L_p = \sum_{\alpha=1}^{12} \dot{\gamma}^\alpha s^\alpha \otimes n^\alpha \quad (2)$$

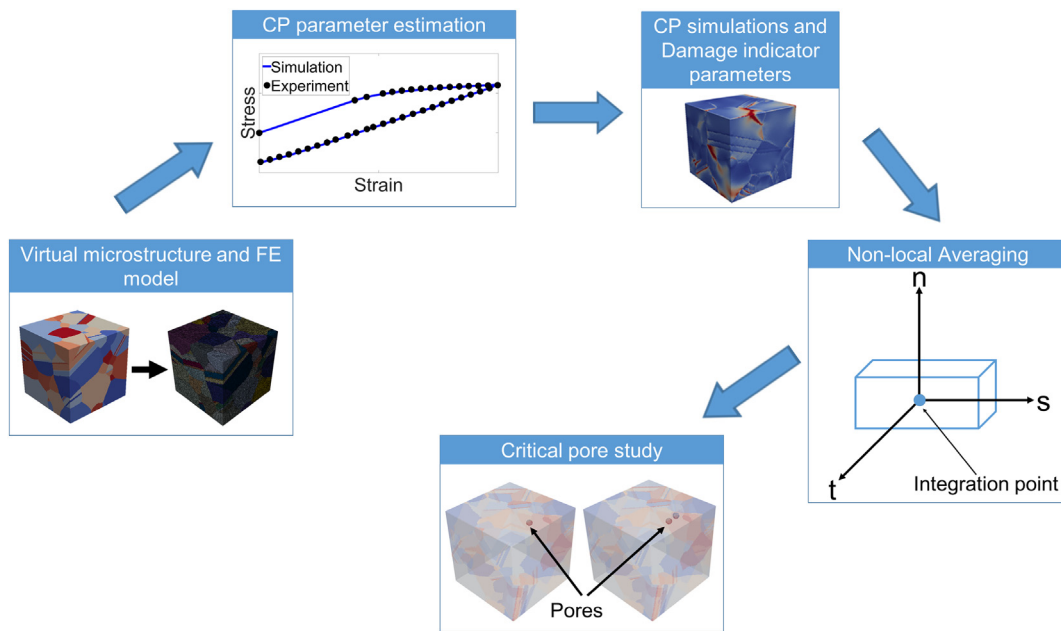


Fig. 3. Modeling framework for the critical pore study which includes creation of 3D virtual microstructures and subsequent generation of finite element meshes, CP parameter estimation using a genetic algorithm, Cyclic FE simulations of microstructural models and estimation of damage indicator parameters, application of non-local averaging, followed by critical pore analyses.

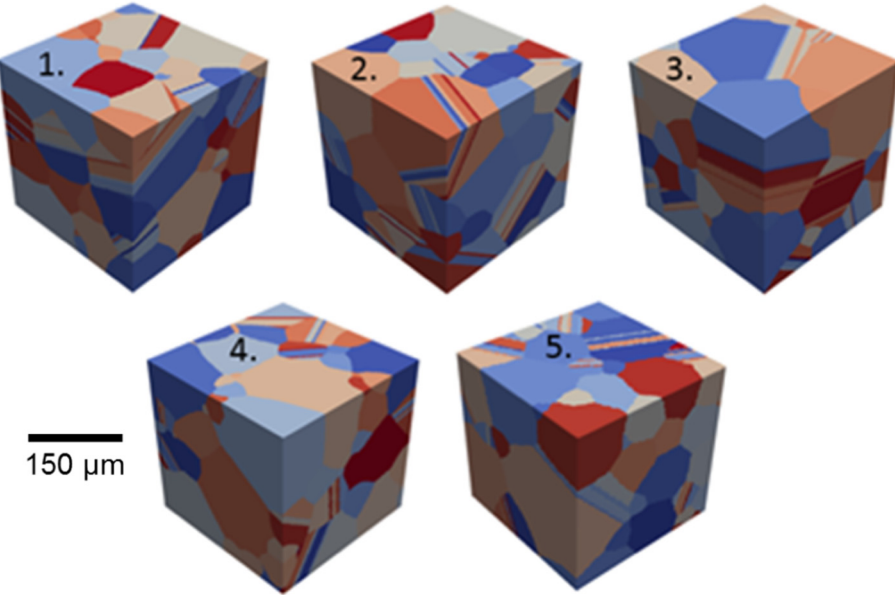


Fig. 4. SEMs used as input to the CP-FE simulations that are statistically representative of the EBSD microstructural attributes and have similar macroscopic strength behavior.

s^α is the slip direction and n^α is the slip normal of the α^{th} slip system. A Hutchinson type flow rule [57] relating the shear strain rates to the resolved shear stress, τ , is used.

$$\dot{\gamma}^\alpha = \dot{\gamma}_0 \left| \frac{\tau^\alpha - \chi^\alpha}{g^\alpha} \right|^m \operatorname{sgn}(\tau^\alpha - \chi^\alpha) \quad (3)$$

$\dot{\gamma}_0$ is the initial shear strain rate, g and χ are the reference stress and back stress, respectively, and m is the rate sensitivity exponent. The evolution laws for the reference stress and the back stress are based on the Armstrong–Frederick type equations [58,59] and are given by:

$$\dot{g}^\alpha = H \sum_{\beta=1}^{12} q^{\alpha\beta} |\dot{\gamma}^\beta| - H_d g^\alpha \sum_{\beta=1}^{12} |\dot{\gamma}^\beta| \quad (4)$$

$$\dot{\chi}^\alpha = A \dot{\gamma}^\alpha - A_d \chi^\alpha |\dot{\gamma}^\alpha| \quad (5)$$

H and H_d are the direct hardening and dynamic recovery coefficients, respectively, for the reference stress. A and A_d are the direct hardening and dynamic recovery coefficients respectively for the back stress. $q^{\alpha\beta}$ is the hardening matrix which has values of 1 for self-hardening (diagonal terms) and 1.2 for latent hardening (off-diagonal terms) [60]. There are 8 crystal plasticity parameters that are calibrated based on the experimental macroscopic stress-strain response. The parameter estimation is posed as an unconstrained minimization problem

with the objective function given by:

$$f = \sqrt{\sum_N w^i (S_{\text{expt}}^i - S_{\text{sim}}^i)^2} \quad (6)$$

w^i , S_{expt}^i , and S_{sim}^i are the weights, experimental stress values, and simulated stress values at the i th point, respectively, and N is the total number of points at specific intervals of strain, in which the stress data is probed. Higher weights are given to the maximum and minimum stress values, in order to properly capture the Bauschinger effect of the material. A genetic algorithm (GA) is used to solve the minimization problem, in order to obtain the CP parameters.

Also, due to the uncertainty in values for the single crystal elastic constants of IN718 in the literature, these constants were obtained by back fitting the elastic portion of the experimental stress-strain response using the GA. The upper and lower bounds for the cubic constants (C_{11} , C_{12} , and C_{44}) for the fit were taken from the literature [61–64]. All the model parameters are shown in Table 3. The model

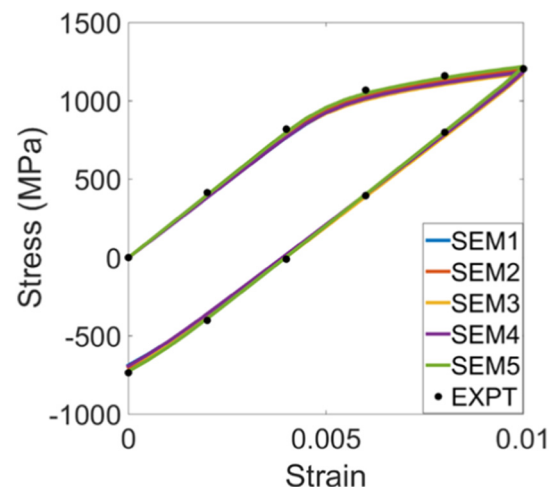


Table 2
Microstructural statistics of the SEMs.

SEM	No. of Grains	Grain sizes (μm)			Twin Area Fraction	Taylor Factor		
		Min	Mean	Max		X	Y	Z
1	205	15	49	203	0.50	3.1	3.0	3.1
2	189	16	47	195	0.50	3.1	3.0	3.1
3	189	17	49	175	0.53	3.1	3.1	3.0
4	190	15	48	209	0.51	3.0	3.1	3.0
5	198	15	46	188	0.50	3.1	3.1	3.1

Fig. 5. Similar macroscopic stress-strain behavior exhibited by the SEMs with the same set of CP parameters.

Table 3
Parameters used in the CP simulations.

No.	Parameters	Values
1	C11	225.7 GPa
2	C12	151.2 GPa
3	C44	112.3 GPa
4	$\dot{\gamma}_0$	0.0004 s ⁻¹
5	m	38
6	g_0	380 MPa
7	H	7800 MPa
8	H_d	19
9	A	14,000 MPa
10	A_d	84
11	χ_0	10 MPa

calibration with the experimental macroscopic stress-strain curve for ten cycles until saturation of the hysteresis loops is shown in Fig. 6.

3.3. Cyclic simulations and damage indicator parameters

Each CP-FE model under investigation is subjected to strain controlled fatigue cycling from 0 to 1%. A total of 47 CP-FE simulations are conducted within this study, and the computational time necessary for each simulation on 160 processors is ~4–5 days. As discussed in Section 4.2, the critical pore size estimation involves a comparison within the spatial distribution of the damage metrics. From a single CP-FE simulation, it was found that the spatial distribution of the damage metrics had a similar trend in terms of the most probable location of failure for both four cycles and ten cycles. Hence, the present analysis based upon the computational costs and identifying the most likely location of crack initiation, relies upon the results of CP-FE simulations after four loading cycles.

The boundary conditions used in the FE simulations are shown in Fig. 7 and are consistent with those proposed in [65]. U_x , U_y , and U_z represent the displacements in x, y, and z directions, respectively. U_x is zero on the $x = 0$ face, U_y is zero on the $y = 0$ face, U_z is zero on the $Z = 0$ face, U_y is specified on the top face (Fig. 7) based on the applied strain values, and the other two faces (X or $Z = 300 \mu\text{m}$) are free. In this work, we are primarily interested in the role of porosity in SLM IN718, and the presence of residual stress gradients and surface roughness effects are not taken into account.

To understand the fatigue behavior, four damage indicator parameters (DIPs) have been calculated in this study based on their prevalence to fatigue crack initiation as previously discussed in [66], namely, the plastic strain accumulation (PSA), elastic stress anisotropy (ESA), change in resolved shear stress (ΔRSS) and the triaxiality (Triax). PSA indicates the localization of plastic slip in the microstructure [67,68] and strain localization is well-known to be a precursor to crack initiation [69,70]. PSA is obtained as the time integral of the scalar product of the

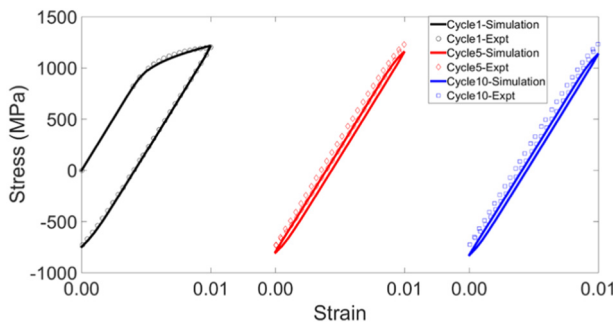


Fig. 6. Comparison of the macroscopic stress-strain behavior of experiments and simulations using calibrated CP parameters until ten cycles.

plastic velocity gradient, L_p ,

$$\dot{p} = \sqrt{\frac{2}{3} L_p : L_p} \quad (7)$$

$$\text{PSA} = \int \dot{p} dt \quad (8)$$

ESA gives a scalar measure of the lattice incompatibility tensor [71] and is representative of the internal stresses caused by geometric mismatch of the slip system at the grain boundary.

$$\alpha = \text{Curl}(F_p) = -\text{curl}(F_e^{-1}) \quad (9)$$

$$\text{ESA} = \sqrt{\frac{3}{2} \alpha : \alpha} \quad (10)$$

RSS provides a measure of the shear stress on a slip system which drives the plastic deformation. ΔRSS is obtained between the maximum and the minimum strain points during a loading cycle, and the value of ΔRSS is taken as the maximum value over the 12 slip systems, β .

$$\tau^\beta = \sigma : (s^\beta \otimes n^\beta) \quad (11)$$

$$\Delta RSS = \max_\beta \Delta \tau^\beta \quad (12)$$

Triax is the ratio of the hydrostatic stress to the equivalent stress. Hydrostatic stress influences the volume change of a material point which is an elastic process. Equivalent (or von Mises) stress is derived from the deviatoric part of the stress tensor and it affects the shape change of a material point. The relevance of triaxiality to crack initiation is discussed in [72].

$$\text{Triax} = \frac{\text{Hydrostatic stress}}{\text{Equivalent stress}} \quad (13)$$

ESA and Triax are obtained at the maximum applied strain point corresponding to the fourth cycle, PSA is obtained at the minimum applied strain point at the fourth cycle, and ΔRSS is obtained across the fourth cycle as a difference between the peak and minimum applied strains.

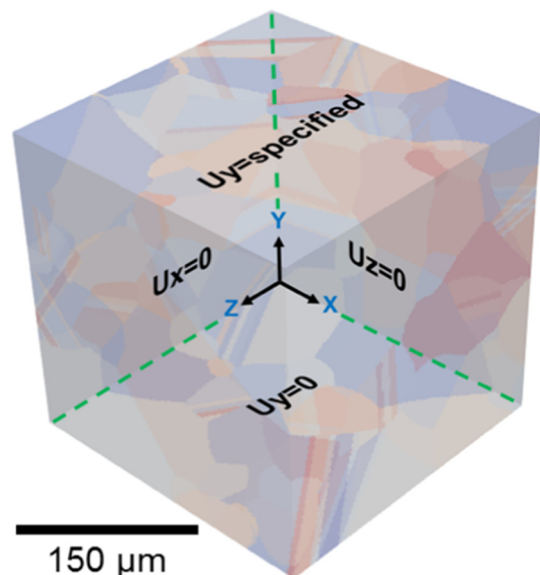


Fig. 7. Displacement boundary conditions applied on the boundary faces of the microstructure model used in the CP-FE simulations. U_x is zero on the $x = 0$ face, U_y is zero on the $y = 0$ face, U_z is zero on the $Z = 0$ face, U_y is specified on the top face, and the other two faces (X or $Z = 300 \mu\text{m}$) are free.

3.4. Non-local averaging

The DIPs obtained from the CP-FE simulations exhibited high oscillatory behavior at a few elements in the microstructure model. These spurious values could be due to one of the following: a) the mesh (highly skewed element) near the grain boundary, b) volumetric locking exhibited by the linear mesh elements [73], or c) the effect of boundary conditions on the surface elements (Fig. 9). To mitigate this, a non-local spatial averaging technique is performed during the post-processing of the resulting micromechanical fields. The non-local averaging is a regularizing scheme that smooths such high oscillations in the values of the DIPs. It also enables a consistent method of reporting DIPs that is less sensitive to the size of the mesh. Castelluccio et al. introduced one such regularization scheme where the averaging is performed within a volume bounded by two adjacent parallel slip planes extending throughout the grain [74]. However, this scheme might not be able to preserve the localization of the micromechanical fields due to the use of a larger averaging volume. Hence, an averaging scheme is introduced over a slip system within a grain which is capable of both smoothing highly oscillatory behavior, as well as preserving localized fields.

In the averaging scheme introduced above, a volume (Fig. 8a), bounded by the slip direction, orthonormal in-plane vector, and slip plane normal around an integration point is considered. All the data inside the volume are averaged and re-assigned to the integration point. Thus, the field values are weighted with respect to their closest neighbors which reduces the oscillations. The maximum averaged value of the DIP among the 12 slip systems is considered for further analysis. In performing the averaging, the volume is not allowed to cross the grain boundary as shown in Fig. 8b. The averaging scheme closely aligns with the physics of slip deformation, thereby retaining the associated gradients in the micromechanical fields. Also, by restricting the averaging domain to be within a grain enables preservation of the gradient developed across the grain boundary due to kinematic compatibility and elastic anisotropy.

The size of the averaging domain is dependent on the local finite element size and is taken as ~3–4 elements with respect to the slip direction and ~2–3 elements in the transverse directions based on a sensitivity study. This volume satisfies the requirement of smoothing spurious values and preserving the localization of the micromechanical fields. The volume corresponding to each integration point would be different due to the restrictions placed on the domain to be within the grain. The maximum possible size corresponds to $10 * 8 * 6 \mu\text{m}^3$. As the same settings are used in all the 47 CP-FE simulations, consistent results are expected.

Fig. 9 shows the comparisons of the stress values along a random probe line in the FE microstructure in the loading direction. The three plots shown in Fig. 9 correspond to the local element values obtained from the coarse mesh, non-local averaged values obtained from the coarse mesh, and the non-local averaged values obtained from the fine mesh. The details of the coarse mesh and the fine mesh are given in Table 4. The smoothing of the stress values due to the application of the averaging technique is evident from Fig. 9 and the mesh sensitivity

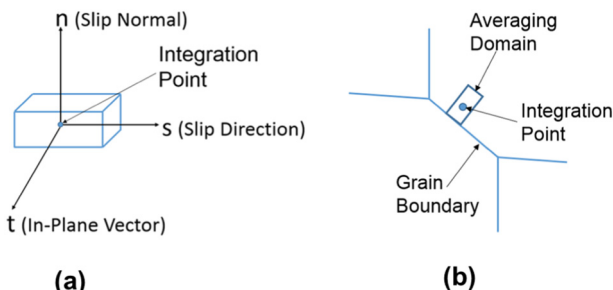


Fig. 8. (a) Averaging volume bounded by slip direction, in-plane vector, and slip plane normal and (b) Averaging domain restricted within a grain.

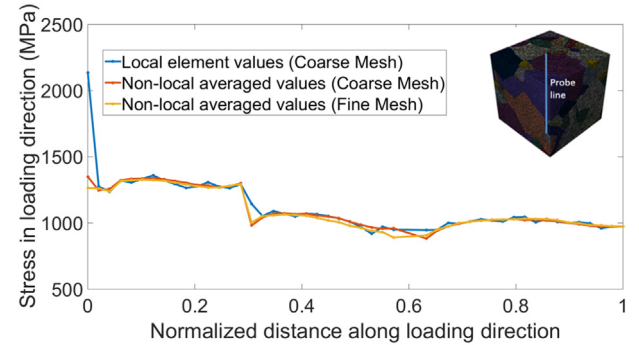


Fig. 9. Comparisons of the stress values along a random probe line evaluated from the local element values of the coarse mesh, non-local averaged values obtained from coarse mesh, and non-local averaged values obtained from fine mesh.

study using the non-local averaged stress values indicate that the coarse mesh shows converged results in comparison to the fine mesh which justifies the choice of the coarse mesh in our simulations.

4. Results

In a polycrystalline microstructure with pores, the fatigue crack may either initiate at a crystallographic feature (grain boundary, triple/quad points, twin boundary, etc.) or at a pore. The goal of the critical pore study is to identify the scenarios under which the fatigue crack is likely to initiate at the pore rather than the crystallographic features.

Further, in this paper, a microstructure with multiple pores will be referred to as a flawed model, a microstructure with no pore will be called a fully dense microstructure. Any micromechanical field quantity (stress, strain, etc.) around a pore in the flawed model depends on the size of the pore, anisotropy of the surrounding grains and the interaction effects (pore-pore and pore-boundary). Mathematically, any micromechanical field (ψ) near a pore could be approximated as:

$$\psi \sim \psi_{\text{avg}} + \Delta\psi_{\text{poresize}} + \Delta\psi_{\text{anisotropy}} + \Delta\psi_{\text{interaction}} \quad (14)$$

$\Delta\psi$ represents the perturbation due to the specified factor.

The critical pore study is formulated as three connected studies based on Eq. (14), namely, the pore placement study with respect to the SEM, critical size study, and the cluster study. Each study accounts for only one factor. The first two studies have a single pore in the microstructure as shown in Fig. 10a, and the cluster study has two pores in the microstructure as shown in Fig. 10b. The pore in the model is created by element deletion from the meshed model. Before deletion, the FE mesh is locally refined at the local neighborhood around the pore center with an element size of $1 \mu\text{m}$. The refinement is carried out within a sphere of radius $10 \mu\text{m}$ greater than the pore radius. This provides a more realistic pore representation and a local refined mesh near the pore to capture gradients in the micromechanical fields. The nearest two layers of elements near the pore are not considered while obtaining the spatial distribution of the DIPs to avoid the effects of the local geometrical serrations caused by element deletion. The descriptions of each study with the mechanistic basis of the formulation and corresponding results are given below.

Table 4

A comparison between the coarse mesh and the fine mesh for the CP-FE models with respect to element size, number of nodes and elements, and computational time for one cycle.

Finite element model	Element Size (μm)	No. of Nodes	No. of Elements	Simulation time for 1 cycle
Coarse Mesh	3.2	0.7 M	3.8 M	~1 day
Fine Mesh	2	2.2 M	13.7 M	~10 days

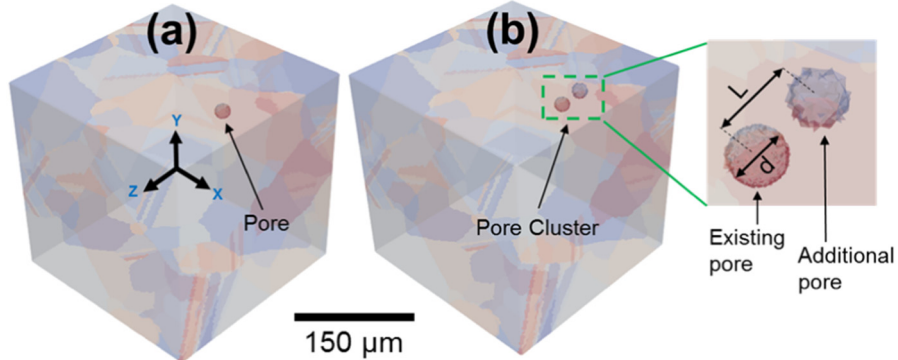


Fig. 10. Representative microstructure models used in the critical pore study with (a) a single pore and (b) two pores.

4.1. Pore placement study

In the pore placement study, the FE microstructures are set up in such a way to include only the influence of the surrounding anisotropy ($\Delta\psi_{anisotropy}$). This is accomplished by following three steps. First, the models are created with a single pore, which eliminates the pore-pore interaction effects. Second, the pore is deliberately placed in the bulk of the microstructure, which reduces the pore-boundary interaction effects, and third, all the models are created with a fixed pore size of 30 μm , which eliminates the effect of the pore size. This study identifies the location in the fully dense microstructure, where a pore should be placed representing the worst-case scenario for a fatigue crack to initiate, as predicted by the DIPs.

It is well known that the intersection points in a fully-dense microstructure (grain boundaries, triple, and quad points) act as stress concentrators. From a study consisting of seven CP-FE simulations, it was found that a pore when placed at the intersection point (of the fully-dense microstructure) possessing the highest stress, resulted in the maximum values of the DIPs (PSA, ΔRSS , and Triax) near the pore. This information regarding the pore placement is used to set up the simulations for the critical size study.

4.2. Critical size study

In the critical size study, the influence of the pore size ($\Delta\psi_{poresize}$) is studied by using only a single pore placed at a fixed location (highest stress intersection point corresponding to each SEM), which eliminates

the anisotropy and interaction effects. For each SEM, five models are created with one pore in each SEM having sizes of 10, 20, 30, 40, and 50 μm respectively. This study estimates the critical pore size corresponding to each SEM, which is defined as the size beyond which the location of crack nucleation, as determined by the values of the resulting DIPs, transitions from crystallographic features to the pore vicinity. From the simulations, the critical size is obtained from the radial distribution function of the maximum values of the non-local averaged DIPs. It is estimated by identifying the pore size at which the DIPs near the pore attain the maximum value as compared to the rest of the microstructure.

The radial distribution function of all the DIPs for each SEM are plotted in Figs. 11–15. The fully dense case (with no pore) is plotted in the figures to have a baseline comparison for the SEM models with a pore. The Figs. 11–15 have the same range for each DIP for all SEMs to enable easier visual comparison. It could be observed that the radial distribution of each DIP corresponding to an SEM is distinct and is predominantly due to the variability of the microstructures across the SEMs. For a single SEM, the DIPs near the pore vicinity are different for each pore size and they converge to the values of the fully-dense case farther from the pore center.

Of all DIPs, both the PSA and ΔRSS have a strong correlation with the pore size as can be seen in Figs. 11–15. In most cases, both the PSA and ΔRSS monotonically increase with an increase in the pore size. In very few cases (as in Fig. 15), there is a slight decrease of both the PSA and ΔRSS while going from a pore size of 40 to a pore size of 50. This could be attributed to a couple of reasons: a) the immediate neighborhood is different for each pore size or b) local refinement in mesh. On

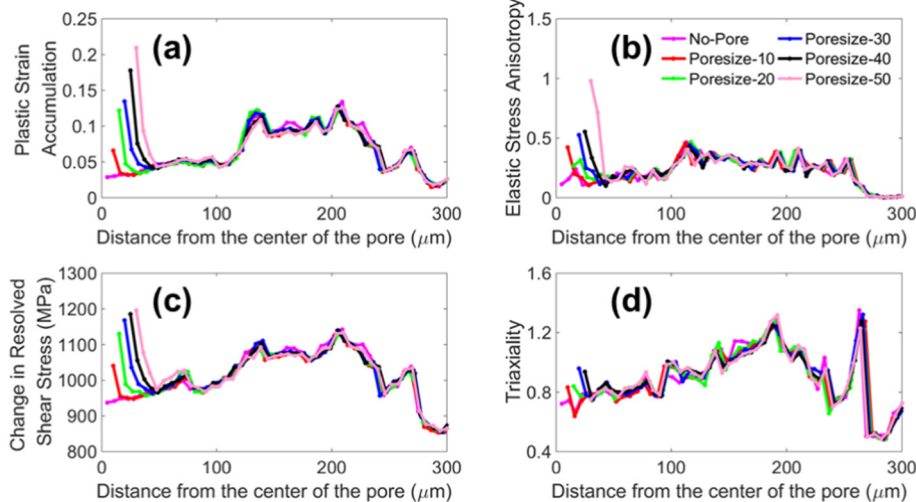


Fig. 11. Radial distribution plots of the damage indicator parameters for SEM1 (a) Plastic strain accumulation, (b) Elastic stress anisotropy, (c) Change in resolved shear stress, and (d) Triaxiality.

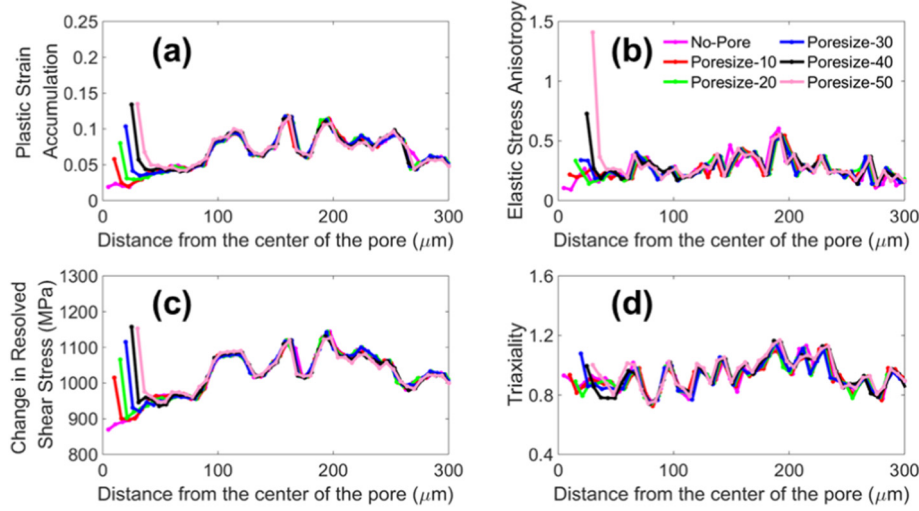


Fig. 12. Radial distribution plots of the damage indicator parameters for SEM2 (a) Plastic strain accumulation, (b) Elastic stress anisotropy, (c) Change in resolved shear stress, and (d) Triaxiality.

the other hand, both the ESA and Triax do not have a strong correlation with the pore size. The ESA involves gradients, which are numerically calculated during post-processing using the following equation [75]

$$\frac{\partial \phi}{\partial x_r} = \frac{\sum_{m=1}^n \frac{1}{r_m} \frac{(\phi_k - \phi_m)}{((x_r)_k - (x_r)_m)}}{\sum_{m=1}^n \frac{1}{r_m}} \quad (15)$$

$\frac{\partial \phi}{\partial x_r}$ is the partial derivative of a field quantity ϕ with respect to a Cartesian coordinate direction x_r . The partial derivative is evaluated at the kth point using the information of the closest n (=10) neighboring points. r_m is the distance between the kth point and the mth neighboring point. ϕ corresponds to the plastic deformation gradient tensor (F_p) in calculating the ESA. Since ESA involves calculations of gradients explicitly, this quantity is more sensitive to the mesh and serrations near the pore, which would explain the inconsistent behavior of the ESA especially near the pore in Figs. 11–15. As for the behavior of the Triax, it could be attributed to the fact that it is a ratio of two different stress

measures. For all the SEMs, the Triax has been observed to be higher at the microstructural features than at the pore vicinity due to the additional volume constraints.

The peak values of all the DIPs, observed particularly near the microstructural features in Figs. 11–15, are not subjected to a detailed investigation to find out the inherent microstructural features, as the focus of this work is more towards the porosity than understanding the microstructural attributes related to fatigue crack initiation.

From the observations above, only the PSA and ΔRSS are considered further in the assessment of the critical pore size. For each SEM, the critical pore size is obtained based on the radial functions of the PSA and ΔRSS. The critical pore size thus obtained for each SEM is plotted in Fig. 16, and it varies from 20 to 40 μm across all the SEMs. As a conservative estimate the critical pore size could be taken as 20 μm, which is ~40% with respect to the average grain size of 48 μm.

The maximum values of the PSA and ΔRSS at the pore vicinity for all the SEMs with respect to pore size is plotted in Fig. 17. For the same pore size, there exists a considerable variation of the resulting PSA and ΔRSS. The deviation in the values could be strongly related to the difference in the surrounding microstructure associated with each SEM around the

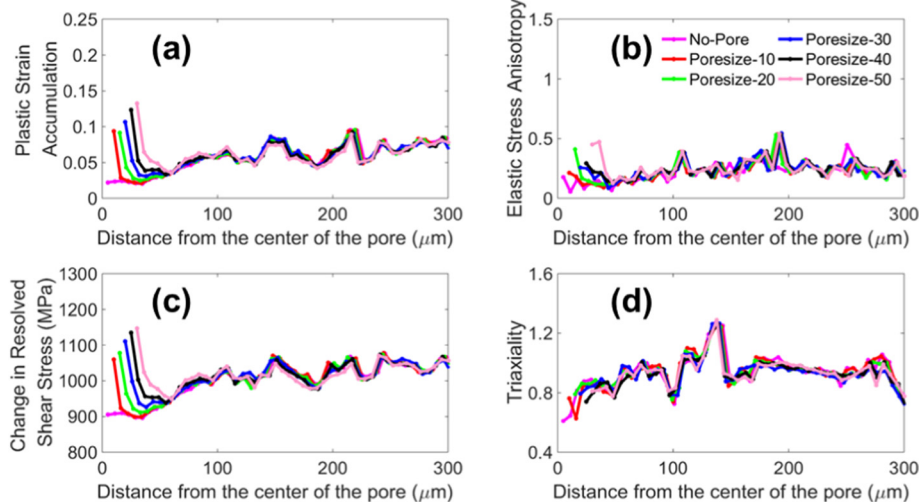


Fig. 13. Radial distribution plots of the damage indicator parameters for SEM3 (a) Plastic strain accumulation, (b) Elastic stress anisotropy, (c) Change in resolved shear stress, and (d) Triaxiality.

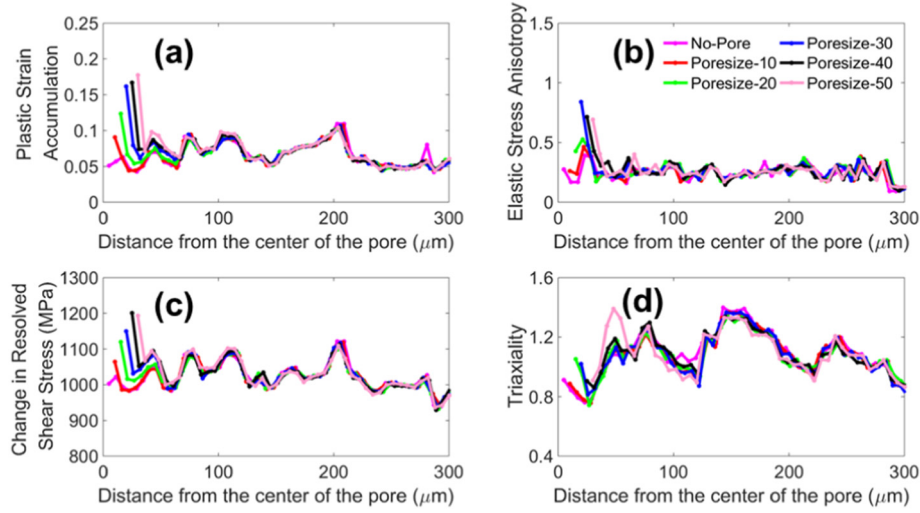


Fig. 14. Radial distribution plots of the damage indicator parameters for SEM4 (a) Plastic strain accumulation, (b) Elastic stress anisotropy, (c) Change in resolved shear stress, and (d) Triaxiality.

pore. Fig. 18 shows the visualization of all the DIPs corresponding to SEM4 with a 20 μm pore. Fig. 18 is mainly intended to depict the heterogeneous deformation behavior of the polycrystalline microstructure and the localization of the micromechanical fields near the pore. Each DIP is plotted with respect to the entire microstructure and about a cross-section across the pore. The PSA, ESA, ΔRSS and Triax are shown in Fig. 18 (a), (b), (c), and (d), respectively.

4.3. Cluster study

In the cluster study, the influence of the pore-pore interaction is studied. All the models in this study have two pores (representing a pore cluster) of the same diameter, d , in the microstructure (Fig. 10b) with their centers separated by a distance of L . The simulations are performed by fixing both the size and location of the existing pore (Fig. 10b) and the position of the additional pore is varied, thereby varying L in each simulation. The cluster study models (Fig. 10b) are created using the critical size study microstructures (Fig. 10a). The additional pore (Fig. 10b) is created on the plane (X-Z) perpendicular to the loading direction (Y) and radially adjacent to the point in the circumference

of the existing pore that has the maximum PSA, which allows for the maximum interaction effects.

From the critical size study, SEM4 has the least critical pore size of 20 μm in terms of both PSA and ΔRSS and hence, it is chosen for the cluster study as it is representative of the worst-case scenario. The first set of cluster models identify the critical separation distance below which a combination of two sub-critical pores ($d = 10 \mu\text{m}$) is likely to initiate a fatigue crack. This is estimated by comparing the simulation results of the pore cluster study with the results of the critical size study.

Figs. 19 (a) and (b) display the variation of the PSA and ΔRSS for various L/d ratios. The critical value in Fig. 19 corresponds to the respective DIP values obtained from the CP-FE simulation of a single 20 μm pore in SEM4 from the critical size study. For the pore cluster of $d = 10 \mu\text{m}$, the PSA (Fig. 19 a) exceeds the critical value when L/d equals 1.5, whereas ΔRSS does not exceed the critical value in any case. With respect to PSA, it could be concluded that when the separation distance, L , is less than or equal to 15 μm , a fatigue crack is likely to initiate at the pore cluster.

The second set of studies are performed with two pores each having a size of 20 μm in order to understand the nature of the pore-pore interaction effects on both the PSA and ΔRSS as a function of L/d .

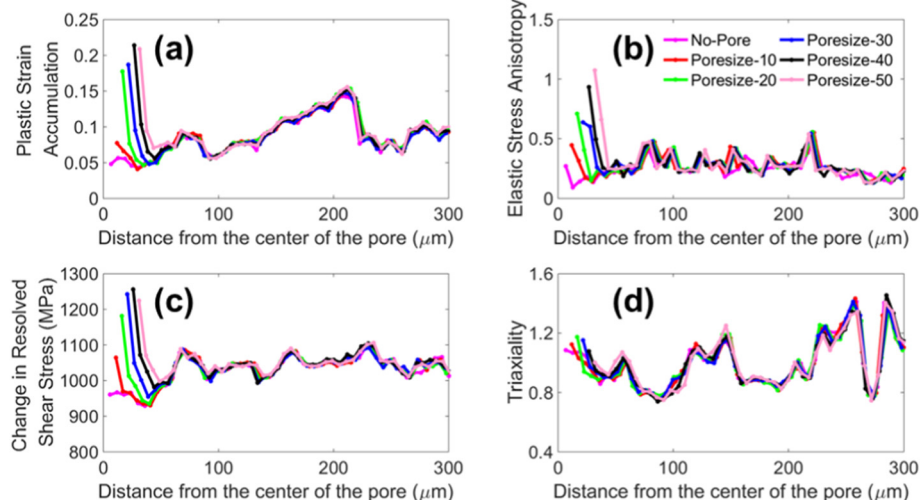


Fig. 15. Radial distribution plots of the damage indicator parameters for SEM5 (a) Plastic strain accumulation, (b) Elastic stress anisotropy, (c) Change in resolved shear stress, and (d) Triaxiality.

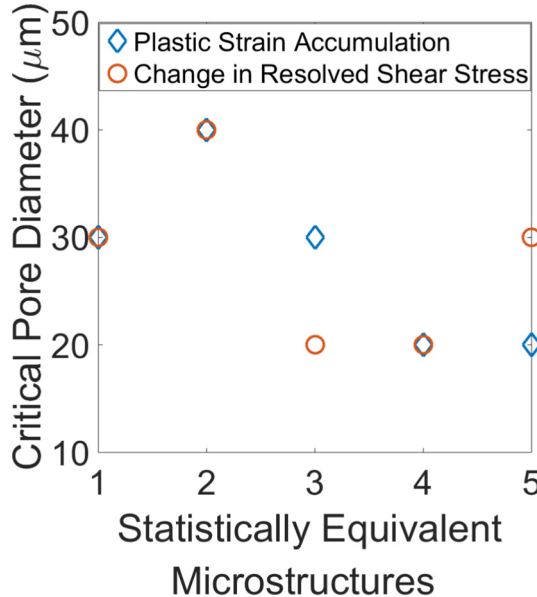


Fig. 16. Critical pore diameter for each SEM with respect to plastic strain accumulation and change in resolved shear stress.

Investigation of Figs. 19 and 20 show that interaction effects are most dominant when L/d ratio is less than or equals 2.

5. Discussion

Based on the results of the CP-FE simulations, the size of a critical single pore to cause a potential debit in the fatigue life of SLM IN718 is determined to be 20 μm. From this conservative assessment, a standalone pore of size 20 μm or greater within the microstructure is likely to initiate a fatigue crack. Moreover, additional pores in the vicinity of the initial critical pore would result in a further detriment to the fatigue life. Even sub-critical pores with diameters of 10 μm could cause fatigue failure when the separation distance between them is less than 15 μm, due to the pore-to-pore interaction. The results of the CP-FE simulations are compared with the μXSCT characterization (Fig. 2) to identify the probability of limiting porosity within representative SLM IN718 material. From Fig. 2, the probability of a single pore greater than 20 μm in size is 0.2%, while the probability of pores possessing a diameter of 10 to 20 μm is equal to 1.8%. In general, the probability of pores being spaced

less than 15 μm apart is 41.6%. From the probability values determined from the μXSCT characterization, based on their size and separation distance, ~1% pores are likely to providing a fatigue debit. For this SLM IN718 material, a tomography measurement with resolution of 10 μm (5 μm voxel size based on Nyquist sampling) would be sufficient for detection of critical porosity within the material. In addition, the process build parameters and subsequent post-processing treatments could be tailored to control the porosity within the critical limits as obtained from the simulation results.

The final mode of failure from a pore is due to the pore-boundary interaction. Although the pore-boundary interactions are not explicitly modeled, it is possible to obtain a rough estimate from the results of the porosity cluster study. Based on symmetry, we propose the approximation as shown in Fig. 21. A pore cluster separated by a distance, L, is idealized into a pore-boundary configuration with a separation of L/2. Of course, the traction free-boundary conditions of the free surface and the resulting surface deformation would result in a breakdown of this simplifying assumption. Nevertheless, the imposed symmetry condition would be more detrimental to the values of the DIPs than the free surface, as the additional out-of-plane constraints from the symmetry condition would result in additional localization of the micromechanical fields compared to the free surface condition. Hence, the symmetry assumption depicted in Fig. 21 provides a conservative estimate. From the cluster study, it was determined that a pore cluster, in which pores are separated by less than 15 μm would provide a debit in the fatigue life and the pore-to-pore interaction would be dominant when the L/d ratio is less than 2. Based on these results, a surface connected pore or pore immediately sub-surface by a distance equivalent to its diameter would result in localization of the micromechanical fields and likely be a site for fatigue crack initiation.

The CP-FE simulations in this study represent an idealized microstructure, which does not introduce residual stresses, non-metallic inclusions [76], surface roughness, as large as (ALA) grain sizes [77], or notches due to geometric discontinuities, which would further reduce the fatigue life and act as a competing failure mechanism in the presence of porosity. Residual stresses have a less significant effect on crack initiation, as post-processing heat treatment significantly reduces them [6]. Surface defects, including surface roughness and surface connected porosity, are another prominent source of crack initiation in SLM materials [10,78,79]. Any surface defect could be modeled as an equivalent sized surface pore [33,36] using the current framework. Thus, by including more representative defects within the simulation, it is anticipated that the critical pore size would increase, as pore induced crack initiation would serve as a competing mechanism with other flaw-mediated sources of failure. Thus, the current study represents a conservative approach (or worst-case scenario) for the critical pore

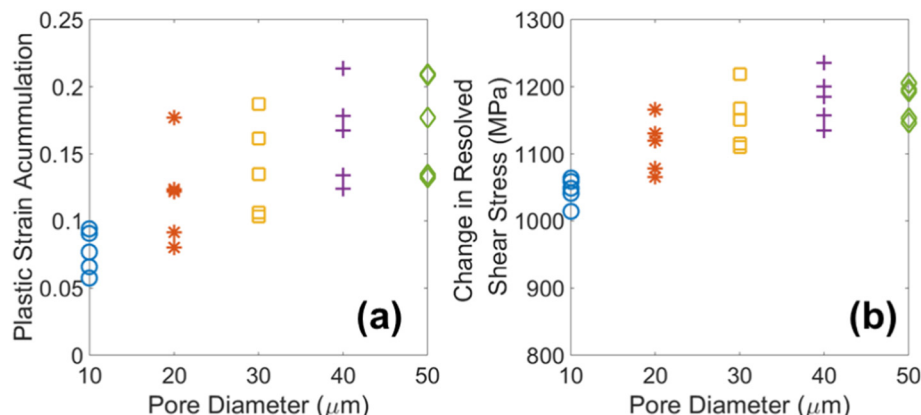


Fig. 17. (a) Plastic strain accumulation, and (b) Change in resolved shear stress at the pore vicinity as a function of pore diameter for all SEMs.

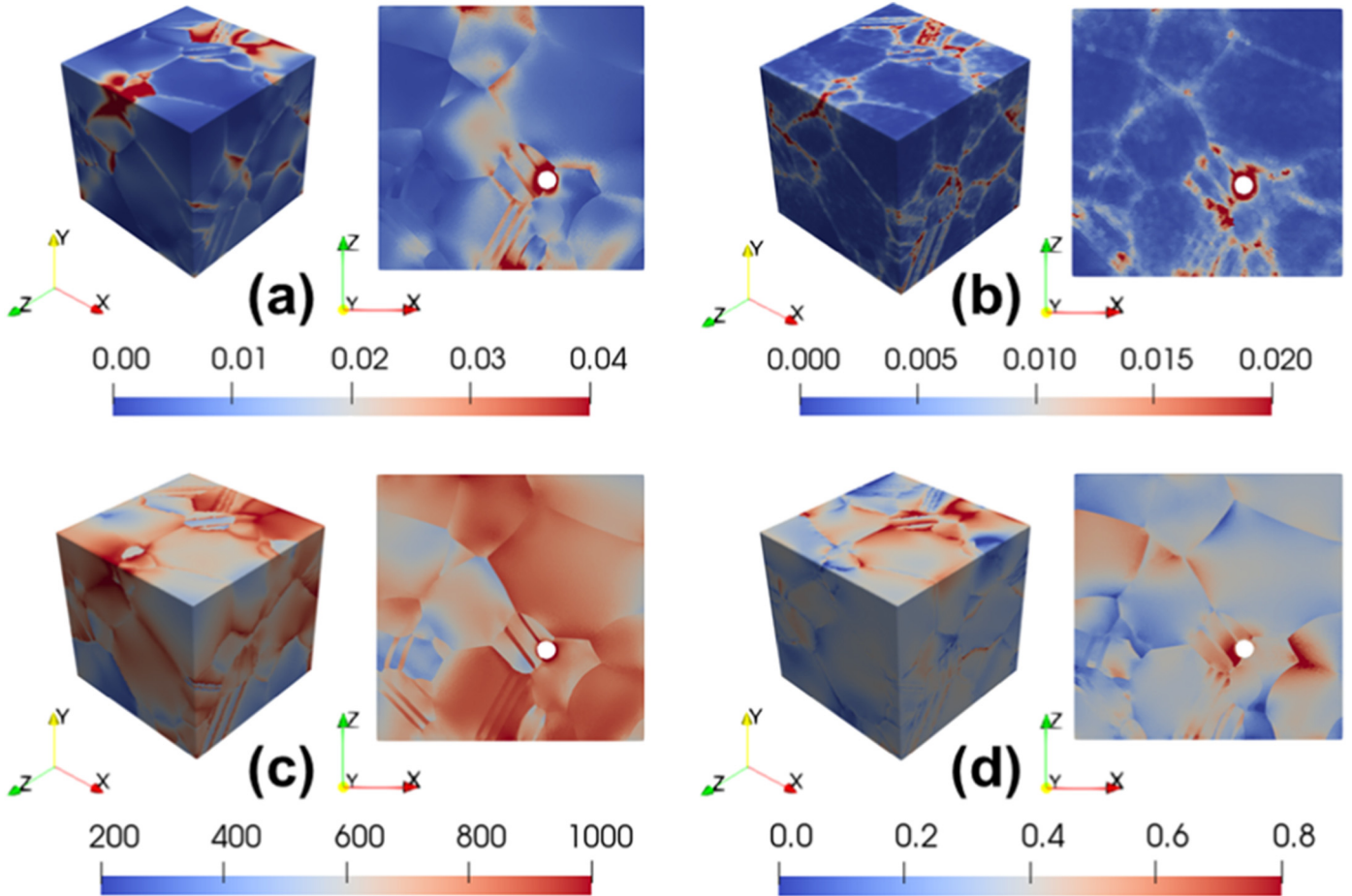


Fig. 18. Visualization of the damage indicator parameters for SEM4 (with 20 μm pore) along with cross-sectional views near the pore showing the spatial variation of (a) Plastic strain accumulation, (b) Elastic stress anisotropy, (c) Change in resolved shear stress, and (d) Triaxiality.

size. As the first attempt at validation, the SLM IN718 material discussed in Section 2 was machined into 8 micro-fatigue specimens with gauge volume of 1 mm^3 . This material, corresponding to the porosity characterization in Fig. 2, was cyclically loaded until failure. Fractography was conducted on the failed fracture surfaces, and in each specimen, porosity was not the cause of failure. Hence, based on the porosity characterization for this material, it was determined from the present modeling analysis that ~1% of the pores in the characterization volume are potentially likely to initiate a fatigue crack, albeit this low percentage was in agreement with the experiments, since pore initiated failure was not observed from the fractography analysis. This is the topic of on-

going research aimed at predicting the fatigue lifetime of SLM IN718 material.

6. Conclusions

- A crystal plasticity based modeling framework is developed to quantify the critical scenarios of porosity towards the fatigue crack initiation of SLM IN718, where,
- Statistical equivalent microstructures are created as input to crystal plasticity simulations which are statistically representative of the microstructural attributes and macroscopic stress response.

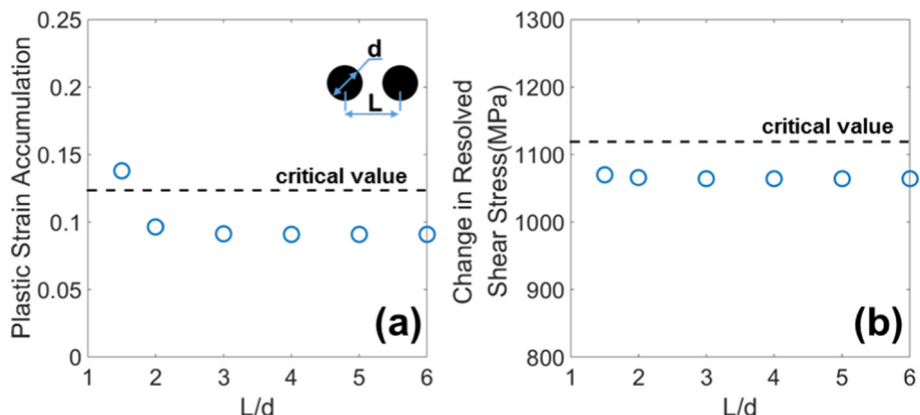


Fig. 19. Variation of the (a) Plastic strain accumulation and (b) Change in resolved shear stress obtained for the cluster study ($d = 10 \mu\text{m}$).

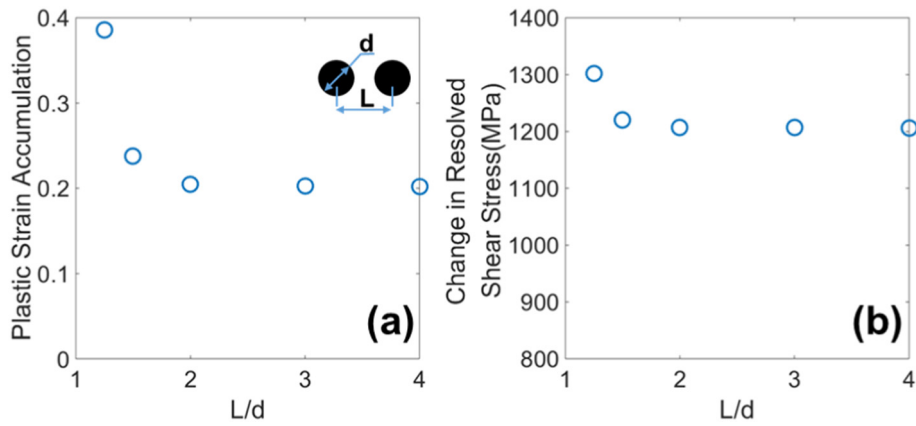


Fig. 20. Variation of the (a) Plastic strain accumulation and (b) Change in resolved shear stress obtained for the cluster study ($d = 20 \mu\text{m}$).

- o Crystal plasticity parameter estimation is posed as an optimization problem and is solved using a genetic algorithm.
- o A spatial non-local averaging technique is introduced to capture the variations of the micromechanical fields, which allows the usage of a coarser mesh.
- o The problem of critical porosity study is formulated as three connected studies based on the mechanics of pore deformation, which are the pore placement relative to the neighboring microstructure, critical size of a single pore, and the separation distance of two pores representing a pore cluster.
- For the SLM IN718 materials with average grain size of $48 \mu\text{m}$, the size of a critical single pore to cause fatigue failure is obtained as $20 \mu\text{m}$. It was also found that even sub-critical pores of $10 \mu\text{m}$ in diameter could cause fatigue failure when the separation distance between these pores is less than $15 \mu\text{m}$, due to the pore-to-pore interaction. Based on a statistical argument, the percentage of critical porosity within the μXSC characterization volume is estimated as ~1%.
- The modeling framework developed in this study has been used to study critical porosity but can be extended to other defects. This work is potentially beneficial in qualifying SLM materials given the natural porosity inherent to the manufacturing process, by reducing the number of necessary fatigue experiments. Additionally, the results of this study can be used to help identify appropriate process build parameters based on the resulting porosity, choice of non-destructive evaluation methods based on the resolution needed to capture the critical pore size, and subsequent post-processing steps necessary to mitigate pores larger than the critical size.

Acknowledgements

This work was financially supported by DARPA (N66001-14-1-4041) under program managers M. Maher and J. Vanderbrande and team: D. Schesser, J. Margiotta, D. Cheng, W. Roy, J. Williams, B. Cowles, R. Martukanitz, and K. Meinert. We thank LTC Todd Book (Purdue) for the EBSD characterization and mechanical testing, Alex Finch (Purdue) for the tomography porosity analysis, Alexandra Mallory (Purdue) for fracture surface analysis, Dr. Xianghui Xiao (Argonne National Laboratory) for his assistance in the set-up of the high resolution tomography analysis, and Peter Coutts (Penn State) for conducting tomography of the parts. Use of the Advanced Photon Source was supported by the US Department of Energy, Office of Science, Office of Basic Energy Sciences, under contract No. DE-AC02-06CH11357.

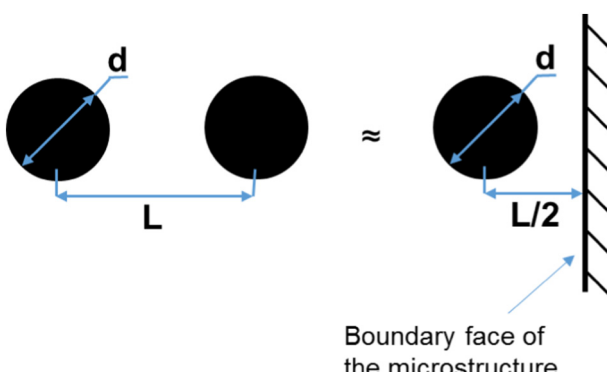
Data availability

Data will be made available upon request.

References

- [1] M. Rombouts, J.P. Kruth, L. Froyen, P. Mercelis, Fundamentals of selective laser melting of alloyed steel powders, *CIRP Ann. Manuf. Technol.* 55 (2006) 187–192, [https://doi.org/10.1016/S0007-8506\(07\)60395-3](https://doi.org/10.1016/S0007-8506(07)60395-3).
- [2] J.P. Kruth, G. Levy, F. Klocke, T.H.C. Childs, Consolidation phenomena in laser and powder-bed based layered manufacturing, *CIRP Ann. Manuf. Technol.* 56 (2007) 730–759, <https://doi.org/10.1016/j.cirp.2007.10.004>.
- [3] L. Thijss, F. Verhaeghe, T. Craeghs, J. Van Humbeeck, J.P. Kruth, A study of the microstructural evolution during selective laser melting of Ti-6Al-4V, *Acta Mater.* 58 (2010) 3303–3312, <https://doi.org/10.1016/j.actamat.2010.02.004>.
- [4] J.P. Choi, G.H. Shin, S. Yang, D.Y. Yang, J.S. Lee, M. Brochu, J.H. Yu, Densification and microstructural investigation of Inconel 718 parts fabricated by selective laser melting, *Powder Technol.* 310 (2017) 60–66, <https://doi.org/10.1016/j.powtec.2017.01.030>.
- [5] H. Gong, K. Rafi, H. Gu, T. Starr, B. Stucker, Analysis of defect generation in Ti-6Al-4V parts made using powder bed fusion additive manufacturing processes, *Addit. Manuf.* 1 (2014) 87–98, <https://doi.org/10.1016/j.addma.2014.08.002>.
- [6] S. Leuders, M. Thöne, A. Riemer, T. Niendorf, T. Tröster, H.A. Richard, H.J. Maier, On the mechanical behaviour of titanium alloy TiAl6V4 manufactured by selective laser melting: Fatigue resistance and crack growth performance, *Int. J. Fatigue* 48 (2013) 300–307, <https://doi.org/10.1016/j.ijfatigue.2012.11.011>.
- [7] G. Strano, L. Hao, R.M. Everson, K.E. Evans, Surface roughness analysis, modelling and prediction in selective laser melting, *J. Mater. Process. Technol.* 213 (2013) 589–597, <https://doi.org/10.1016/j.jmatprotec.2012.11.011>.
- [8] N.T. Aboulkhair, I. Maskery, C. Tuck, I. Ashcroft, N.M. Everitt, Improving the fatigue behaviour of a selectively laser melted aluminium alloy: influence of heat treatment and surface quality, *Mater. Des.* 104 (2016) 174–182, <https://doi.org/10.1016/j.matdes.2016.05.041>.
- [9] J. Günther, S. Leuders, P. Koppa, T. Tröster, S. Henkel, H. Biermann, T. Niendorf, On the effect of internal channels and surface roughness on the high-cycle fatigue performance of Ti-6Al-4V processed by SLM, *Mater. Des.* 143 (2018) 1–11, <https://doi.org/10.1016/j.matdes.2018.01.042>.
- [10] G. Kasperovich, J. Haubrich, J. Gussone, G. Requena, Correlation between porosity and processing parameters in TiAl6V4 produced by selective laser melting, *Mater. Des.* 105 (2016) 160–170, <https://doi.org/10.1016/j.matdes.2016.05.070>.

Fig. 21. Approximating pore-pore interaction to an equivalent pore-boundary interaction.



- [11] P. Edwards, M. Ramulu, Fatigue performance evaluation of selective laser melted Ti-6Al-4V, *Mater. Sci. Eng. A* 598 (2014) 327–337, <https://doi.org/10.1016/j.msea.2014.01.041>.
- [12] S. Tammas-Williams, P.J. Withers, I. Todd, P.B. Prangnell, The influence of porosity on fatigue crack initiation in additively manufactured titanium components, *Sci. Rep.* 7 (2017) 1–13, <https://doi.org/10.1038/s41598-017-06504-5>.
- [13] E. Brandl, U. Heckenberger, V. Holzinger, D. Buchbinder, Additive manufactured AlSi10Mg samples using selective laser melting (SLM): microstructure, high cycle fatigue, and fracture behavior, *Mater. Des.* 34 (2012) 159–169, <https://doi.org/10.1016/j.matdes.2011.07.067>.
- [14] M.J. Couper, A.E. Neeson, J.R. Griffiths, Casting defects and the fatigue behaviour of an aluminium casting alloy, *Fatigue Fract. Eng. Mater. Struct.* 13 (1990) 213–227, <https://doi.org/10.1111/j.1460-2695.1990.tb00594.x>.
- [15] Q.G. Wang, D. Apelian, D.A. Lados, Fatigue behavior of A356-T6 aluminum cast alloys. Part I. Effect of casting defects, *J. Light. Met.* 1 (2001) 73–84, [https://doi.org/10.1016/S1471-5317\(00\)00008-0](https://doi.org/10.1016/S1471-5317(00)00008-0).
- [16] H. Danninger, B. Weiss, The influence of defects on high cycle fatigue of metallic materials, *J. Mater. Process. Technol.* 143–144 (2003) 179–184, [https://doi.org/10.1016/S0924-0136\(03\)00409-6](https://doi.org/10.1016/S0924-0136(03)00409-6).
- [17] S.J. Polaski, J.J. Williams, N. Chawla, Fatigue crack initiation and propagation of binder-treated powder metallurgy steels, *Metall. Mater. Trans. A* 33 (2002) 73–81, <https://doi.org/10.1007/s11661-002-0006-8>.
- [18] H.T. Pang, P.A.S. Reed, Fatigue crack initiation and short crack growth in nickel-base turbine disc alloys – the effects of microstructure and operating parameters, *Int. J. Fatigue* 25 (2003) 1089–1099, [https://doi.org/10.1016/S0142-1123\(03\)00146-4](https://doi.org/10.1016/S0142-1123(03)00146-4).
- [19] S. Dezecot, J.Y. Buffiere, A. Koster, V. Maurel, F. Szmytka, E. Charkaluk, N. Dahdah, A. El Bartali, N. Limodin, J.F. Witz, In situ 3D characterization of high temperature fatigue damage mechanisms in a cast aluminum alloy using synchrotron X-ray tomography, *Scr. Mater.* 113 (2016) 254–258, <https://doi.org/10.1016/j.scriptamat.2015.11.017>.
- [20] S. Benedictus-deVries, A. Bakker, G.C.A.M. Janssen, H. de Wit, Fatigue crack initiation behavior of welded AA5083 in a seawater environment, *J. Eng. Mater. Technol.* 126 (2004) 199, <https://doi.org/10.1115/1.1651098>.
- [21] X. Zhou, D. Wang, X. Liu, D.D. Zhang, S. Qu, J. Ma, G. London, Z. Shen, W. Liu, 3D-imaging of selective laser melting defects in a Co-Cr-Mo alloy by synchrotron radiation micro-CT, *Acta Mater.* 98 (2015) 1–16, <https://doi.org/10.1016/j.actamat.2015.07.014>.
- [22] R. Cunningham, S.P. Narra, C. Montgomery, J. Beuth, A.D. Rollett, Synchrotron-based X-ray microtomography characterization of the effect of processing variables on porosity formation in laser power-bed additive manufacturing of Ti-6Al-4V, *JOM* 69 (2017) 479–484, <https://doi.org/10.1007/s11837-016-2234-1>.
- [23] S. Siddique, M. Imran, M. Rauer, M. Kaloudis, E. Wycisk, C. Emmelmann, F. Walther, Computed tomography for characterization of fatigue performance of selective laser melted parts, *Mater. Des.* 83 (2015) 661–669, <https://doi.org/10.1016/j.matdes.2015.06.063>.
- [24] R. Cunningham, A. Nicolas, J. Madsen, E. Fodran, E. Anagnostou, M.D. Sangid, A.D. Rollett, Analyzing the effects of powder and post-processing on porosity and properties of electron beam melted Ti-6Al-4V, *Math. Res. Lett.* 5 (2017) 516–525, <https://doi.org/10.1080/21663831.2017.1340911>.
- [25] S. Khademzadeh, S. Carmignato, N. Parvin, F. Zanini, P.F. Bariani, Micro porosity analysis in additive manufactured NiTi parts using micro computed tomography and electron microscopy, *Mater. Des.* 90 (2016) 745–752, <https://doi.org/10.1016/j.matdes.2015.10.161>.
- [26] K. Jurrens, Energistics incorporated, measurement science roadmap for metal-based additive manufacturing, *Addit. Manuf.* 86 (2013) <https://doi.org/10.1007/s13398-014-0173-7.2>.
- [27] F.A. McClintock, A criterion for ductile fracture by the growth of holes, *J. Appl. Mech.* (1968) 363–371.
- [28] J.R. Rice, D.M. Tracey, On the ductile enlargement of voids in triaxial stress fields*, *J. Mech. Phys. Solids* 17 (1969) 201–217, [https://doi.org/10.1016/0022-5096\(69\)90033-7](https://doi.org/10.1016/0022-5096(69)90033-7).
- [29] A. Needleman, Void Growth in an Elastic-plastic Medium, 1, 1972 <https://doi.org/10.1115/1.3422899>.
- [30] A.L. Gurson, Continuum theory of ductile rupture by void nucleation and growth: part I—yield criteria and flow rules for porous ductile media, *J. Eng. Mater. Technol.* 99 (1977) 2, <https://doi.org/10.1115/1.3443401>.
- [31] V. Tvergaard, On Localization in Ductile Materials Containing Spherical Voids.pdf, 18, 1982 237–252.
- [32] J. Koplik, a. Needleman, Void growth and coalescence in porous plastic solids, *Int. J. Solids Struct.* 24 (1988) 835–853, [https://doi.org/10.1016/0020-7683\(88\)90051-0](https://doi.org/10.1016/0020-7683(88)90051-0).
- [33] K. Gall, M.F. Horstemeyer, B.W. Degner, D.L. McDowell, J. Fan, On the driving force for fatigue crack formation from inclusions and voids in a cast A356 aluminum alloy, *Int. J. Fract.* 108 (2001) 207–233, <https://doi.org/10.1023/A:101103304600>.
- [34] J. Fan, D.L. McDowell, M.F. Horstemeyer, K. Gall, Cyclic plasticity at pores and inclusions in cast Al-Si alloys, *Eng. Fract. Mech.* 70 (2003) 1281–1302, [https://doi.org/10.1016/S0013-7944\(02\)00097-8](https://doi.org/10.1016/S0013-7944(02)00097-8).
- [35] Z. Xu, W. Wen, T. Zhai, Effects of pore position in depth on stress/strain concentration and fatigue crack initiation, *Metall. Mater. Trans. A Phys. Metall. Mater. Sci.* 43 (2012) 2763–2770, <https://doi.org/10.1007/s11661-011-0947-x>.
- [36] P. Baicchi, G. Nicoletto, E. Riva, Modeling the Influence of Pores on Fatigue Crack Initiation in a Cast Al-Si Alloy, *Int. Conf. CRACK PATHS 2006*, 2006 2–9 http://www.gruppofrattura.it/index.php?option=com_docman&task=doc_download&gid=152&Itemid=228.
- [37] H. Gao, Z. Zhang, Y. Lai, J. Li, Y. Liu, Influence of crystallographic orientation on growth behavior of spherical voids, *J. Cent. S. Univ. Technol.* 15 (2008) 830–834, <https://doi.org/10.1007/s11771>.
- [38] J.D. Carroll, L.N. Brewer, C.C. Battaile, B.L. Boyce, J.M. Emery, The effect of grain size on local deformation near a void-like stress concentration, *Int. J. Plast.* 39 (2012) 46–60, <https://doi.org/10.1016/j.ijplas.2012.06.002>.
- [39] C.C. Battaile, J.M. Emery, L.N. Brewer, B.L. Boyce, Crystal plasticity simulations of microstructure-induced uncertainty in strain concentration near voids in brass, *Philos. Mag.* 95 (2015) 1069–1079, <https://doi.org/10.1080/14786435.2015.1009958>.
- [40] https://www.eos.info/systems_solutions/metal/systems_equipment/eosint_m280.
- [41] Y.S. Yoo, T. Book, M.D. Sangid, J. Kacher, Identifying strain localization and dislocation processes in fatigued Inconel 718 manufactured from selective laser melting, *Mater. Sci. Eng. A* 724 (2018) 444–451, <https://doi.org/10.1016/j.msea.2018.03.127>.
- [42] M.D. Sangid, T.A. Book, D. Naragani, J. Rotella, P. Ravi, A. Finch, P. Kenesei, J.-S. Park, H. Sharma, J. Almer, X. Xiao, Role of Heat Treatment and Build Orientation in the Microstructure Sensitive Deformation Characteristics of IN718 Produced Via SLM Additive Manufacturing(Under Rev.) 2018.
- [43] B.A. Dowd, G.H. Campbell, R.B. Marr, V. Nagarkar, S. Tipnis, L. Axe, D.P. Siddons, Developments in synchrotron X-ray computed microtomography at the National Synchrotron Light Source, *Proc. SPIE*, Society of Photo-Optical Instrument, Bellingham, WA, 1999 <https://doi.org/10.1117/12.363725>.
- [44] M.L. Rivers, tomoRecon: high-speed tomography reconstruction on workstations using multi-threading, *Proc. SPIE* (2012) <https://doi.org/10.1117/12.930022>.
- [45] D. Gürsoy, F. De Carlo, X. Xiao, C. Jacobsen, TomoPy: a framework for the analysis of synchrotron tomographic data, *J. Synchrotron Radiat.* 21 (2014) 1188–1193, <https://doi.org/10.1107/S1600577514013939>.
- [46] N. Otsu, A threshold selection method from gray-level histograms, *IEEE Trans. Syst. Man Cybern.* 9 (1979) 62–66, <https://doi.org/10.1109/TSMC.1979.4310076>.
- [47] C.T. Rueden, J. Schindelin, M.C. Hiner, B.E. DeZonia, A.E. Walter, E.T. Arena, K.W. Eliceiri, ImageJ2: ImageJ for the next generation of scientific image data, *BMC Bioinf.* 18 (2017) 1–26, <https://doi.org/10.1186/s12859-017-1934-z>.
- [48] C.A. Schneider, W.S. Rasband, K.W. Eliceiri, NIH image to ImageJ: 25 years of image analysis, *Nat. Methods* 9 (2012) 671–675, <https://doi.org/10.1038/nmeth.2089>.
- [49] Z. Konrad, User's Guide – Avizo, 2017.
- [50] M.A. Groeber, M.A. Jackson, DREAM. 3D: a digital representation environment for the analysis of microstructure in 3D, *Integr. Mater. Manuf. Innov.* (2014) 1–17.
- [51] L.H. Chan, Synthetic Three-Dimensional Voxel-Based Microstructures that Contain Annealing Twins, Carnegie Mellon University, 2010.
- [52] C. Geuzaine, J.-F. Remacle, Gmsh: a three-dimensional finite element mesh generator with built-in pre-and post-processing facilities, *Int. J. Numer. Methods Eng.* 79 (11) (2009) 1309–1331, <https://doi.org/10.1002/nme.2579>.
- [53] R.J. Asaro, Crystal plasticity, *J. Appl. Mech.* 50 (1983) 921, <https://doi.org/10.1115/1.3167205>.
- [54] L. Anand, M. Kothari, A computational procedure for rate-independent crystal plasticity, *J. Mech. Phys. Solids* 44 (1996) 525–558, [https://doi.org/10.1016/0022-5096\(96\)00001-4](https://doi.org/10.1016/0022-5096(96)00001-4).
- [55] F. Roters, P. Eisenlohr, L. Hantcherli, D.D. Tjahjanto, T.R. Bieler, D. Raabe, Overview of constitutive laws, kinematics, homogenization and multiscale methods in crystal plasticity finite-element modeling: theory, experiments, applications, *Acta Mater.* 58 (2010) 1152–1211, <https://doi.org/10.1016/j.actamat.2009.10.058>.
- [56] E.H. Lee, Elastic-plastic deformation at finite strains, *J. Appl. Mech.* 36 (1) (1969) <https://doi.org/10.1115/1.3564580>.
- [57] J.W. Hutchinson, Creep and Plasticity of Hexagonal Polycrystals as Related to Single Crystal Slip, 8, 1977 1465–1469.
- [58] C.O. Frederick, P.J. Armstrong, A Mathematical Representation of the Multiaxial Bauschinger Effect a Mathematical Representation of the Multiaxial Bauschinger Effect, 3409, 1966 <https://doi.org/10.3184/096034007X207589>.
- [59] M.F. Horstemeyer, D.L. McDowell, R.D. McGinty, Design of experiments for constitutive model selection: application to polycrystal elastoviscoplasticity, *Model. Simul. Mater. Sci. Eng.* 7 (1999) 253–273.
- [60] U.F. Kocks, The relation between polycrystal deformation and single-crystal deformation, *Metall. Mater. Trans. A* 1 (1970) 1121–1143, <https://doi.org/10.1007/BF02900224>.
- [61] C. Ye, J. Chen, M. Xu, X. Wei, H. Lu, Multi-scale simulation of nanoindentation on cast Inconel 718 and NbC precipitate for mechanical properties prediction, *Mater. Sci. Eng. A* 662 (2016) 385–394, <https://doi.org/10.1016/j.msea.2016.03.081>.
- [62] E. Salvati, T. Sui, A.M. Korsunsky, Uncertainty quantification of residual stress evaluation by the FIB-DIC ring-core method due to elastic anisotropy effects, *Int. J. Solids Struct.* 87 (2016) 61–69, <https://doi.org/10.1016/j.ijsolstr.2016.02.031>.
- [63] G. Martin, N. Ochoa, K. Sai, E. Hervé-Luanco, G. Caillietaud, A multiscale model for the elastoviscoplastic behavior of directionally solidified alloys: application to FE structural computations, *Int. J. Solids Struct.* 51 (2014) 1175–1187, <https://doi.org/10.1016/j.ijsolstr.2013.12.013>.
- [64] P. Haldipur, F.J. Margetan, R.B. Thompson, Estimation of Single-Crystal Elastic Constants From Ultrasonic Measurements on Polycrystalline Specimens, 1061, 2006.
- [65] Z. Zhang, M.A. Cuddihy, F.P.E. Dunne, On rate-dependent polycrystal deformation: the temperature sensitivity of cold dwell fatigue, *Proc. R. Soc. A Math. Phys. Eng. Sci.* 471 (2015) <https://doi.org/10.1098/rspa.2015.0214> (pg. 20150214).
- [66] S.R. Yeratapally, M.G. Glavicic, M. Hardy, M.D. Sangid, Microstructure based fatigue life prediction framework for polycrystalline nickel-base superalloys with emphasis on the role played by twin boundaries in crack initiation, *Acta Mater.* 107 (2016) 152–167, <https://doi.org/10.1016/j.actamat.2016.01.038>.
- [67] A. Manonkul, F.P.E. Dunne, High- and low-cycle fatigue crack initiation using polycrystal plasticity, *Proc. R. Soc. A Math. Phys. Eng. Sci.* 460 (2004) 1881–1903, <https://doi.org/10.1098/rspa.2003.1258>.
- [68] C.A. Sweeney, W. Vorster, S.B. Leen, E. Sakurada, P.E. McHugh, F.P.E. Dunne, The role of elastic anisotropy, length scale and crystallographic slip in fatigue crack nucleation, *J. Mech. Phys. Solids* 61 (2013) 1224–1240, <https://doi.org/10.1016/j.jmps.2013.01.001>.

- [69] M.D. Sangid, The physics of fatigue crack initiation, *Int. J. Fatigue* 57 (2013) 58–72, <https://doi.org/10.1016/j.ijfatigue.2012.10.009>.
- [70] S.D. Antolovich, R.W. Armstrong, Plastic strain localization in metals: origins and consequences, *Prog. Mater. Sci.* 59 (2014) 1–160, <https://doi.org/10.1016/j.pmatsci.2013.06.001>.
- [71] A. Acharya, J.L. Bassani, Lattice incompatibility and a gradient theory of crystal plasticity, *J. Mech. Phys. Solids* 48 (2000) 1565–1595, [https://doi.org/10.1016/S0022-5096\(99\)00075-7](https://doi.org/10.1016/S0022-5096(99)00075-7).
- [72] D. Naraganji, M.D. Sangid, P.A. Shade, J.C. Schuren, H. Sharma, J.S. Park, P. Kenesei, J.V. Bernier, T.J. Turner, I. Parr, Investigation of fatigue crack initiation from a non-metallic inclusion via high energy x-ray diffraction microscopy, *Acta Mater.* 137 (2017) 71–84, <https://doi.org/10.1016/j.actamat.2017.07.027>.
- [73] J. Cheng, A. Shahba, S. Ghosh, Stabilized tetrahedral elements for crystal plasticity finite element analysis overcoming volumetric locking, *Comput. Mech.* 57 (2016) 733–753, <https://doi.org/10.1007/s00466-016-1258-2>.
- [74] G.M. Castelluccio, D.L. McDowell, Microstructure and mesh sensitivities of meso-scale surrogate driving force measures for transgranular fatigue cracks in polycrystals, *Mater. Sci. Eng. A* 639 (2015) 626–639, <https://doi.org/10.1016/j.msea.2015.05.048>.
- [75] K. Kirane, S. Ghosh, A cold dwell fatigue crack nucleation criterion for polycrystalline Ti-6242 using grain-level crystal plasticity FE model, *Int. J. Fatigue* 30 (2008) 2127–2139, <https://doi.org/10.1016/j.ijfatigue.2008.05.026>.
- [76] M.J. Caton, S.K. Jha, A.H. Rosenberger, J.M. Larsen, Divergence of mechanisms and the effect on the fatigue life variability of Rene' 88 DT, *Superalloys* (2004) 305–312.
- [77] M.D. Sangid, H.J. Maier, H. Sehitoglu, An energy-based microstructure model to account for fatigue scatter in polycrystals, *J. Mech. Phys. Solids* 59 (2011) 595–609, <https://doi.org/10.1016/j.jmps.2010.12.014>.
- [78] L. Huynh, J. Rotella, M.D. Sangid, Fatigue behavior of IN718 microtrusses produced via additive manufacturing, *Mater. Des.* 105 (2016) 278–289, <https://doi.org/10.1016/j.matdes.2016.05.032>.
- [79] C.A. Kantzos, R.W. Cunningham, V. Tari, A.D. Rollett, Characterization of metal additive manufacturing surfaces using synchrotron X-ray CT and micromechanical modeling, *Comput. Mech.* (2017) <https://doi.org/10.1007/s00466-017-1531-z>.